Characterization of a silicon nitride ceramic material for ceramic springs

Iyas Khader[a,b], Christof Koplin[a], Christian Schröder[a], Jens Stockmann[c], Wieland Beckert[c], Willy Kunz[c], Andreas Kailer[a]

[a] Fraunhofer Institute for Mechanics of Materials IWM, Wöhlerstraße 11, 79108 Freiburg, Germany

[b] Department of Industrial Engineering, German-Jordanian University, P.O. Box 35247, 11180 Amman, Jordan

[c] Fraunhofer Institute for Ceramic Technologies and Systems IKTS, Winterbergstraße 28, 01277 Dresden, Germany

Abstract

Under extreme working conditions such as high temperature, strong electric and magnetic fields and acidic or basic environments, ceramic springs offer a clear advantage over conventional steel springs. In this study, a tailored grade of silicon nitride ceramic was characterized as spring material. The basic characterization was complemented with component tests. Bend bars, helical springs and conical disk springs were manufactured and tested under various loading scenarios.

Manifested by the smallest effective volume of the three tested geometries, helical springs showed the highest fatigue strength. Nevertheless, the complexity involved in manufacturing helical springs pertaining to their geometrical features resulted in a relatively large scatter in fatigue data. The results pointed out the importance of proper design and machining of the contact surface edges in disk springs, which bear the highest stresses.

This work demonstrates the potential of producing ceramic springs with broad applicability and sufficient strength and fatigue resistance.

Keywords: ceramic springs; helical springs; disk springs; high temperature fatigue; silicon nitride

1. Introduction

Advanced engineering ceramic materials have proven their superior mechanical, thermophysical and chemical properties in a wide range of industrial applications. Although highly dependent on the material system under consideration, engineering ceramics generally possess high stiffness and high strength and hardness over a wide range of temperatures. They also exhibit low thermal expansion coefficients, exceptionally low densities, high resistance to wear and contact fatigue and low adhesion affinity to metals. Nowadays, advanced ceramics are standard materials for components and tools that are exposed to severe mechanical, thermal and tribological loads [1, 2, 3, 4, 5, 6, 7, 8, 9, 10]. The application of advanced ceramics is widely found in biomaterials [11, 12, 13, 14, 15, 16], metal cutting [17, 18, 19,

20, 21, 22, 23, 24], metalforming [25, 26, 27, 28, 29] and other manufacturing tools [30] and machine components such as valves, pistons, screws, gears and bearings. At high temperatures and in corrosive environments ceramics offer a viable alternative to metals. For instance, silicon nitride ceramics have been successfully applied up to their glass transition temperature of approx. 950 °C [31]. Ceramic springs show further advantages of being electrically insulating and non-magnetic; thus, significantly expand their field of applications. Notwithstanding their advantages, a thorough knowledge of their fatigue behavior is crucial for designing reliable components.

Standardized fatigue tests on ceramic samples are typically carried out at a positive load ratio R (where $R = \sigma_{min}/\sigma_{max}$), which means that on a particular surface, the material will be subjected to either fluctuating tensile or compressive stress. This approach is followed due to the difficulty of loading a bend bar in a fully reversible mode. Previous studies [32, 33, 34, 35, 36, 37] reported that fatigue starts much earlier with a decreasing stress ratio. Few exceptions are found in the literature [38, 39, 34], in which fatigue tests on bend bars were carried out under fully reversible load. The results obtained by Lube et al. [38] manifested a distinct failure behavior for each loading regime. Under fluctuating tensile loading ($R = 0.1$), the microstructure showed transgranular fracture in addition to β-Si_3N_4 grain pullout suggesting intergranular fracture. On the other hand, the samples loaded with fully reversible load ($R = -1$) clearly showed signs of localized wear and debris formation (typical for fatigue crack propagation in ceramics as observed by Reece et al. [34] and Jacobs and Chen [33]), which may have caused wedging effect at the crack faces, thus, leading to further crack propagation during the compression component of the loading cycle.

In general, fatigue lifetime predictions in ceramics are based on the assumption that macroscopic cracks develop from natural flaws associated with preexisting defects under cyclic loading. It was shown by means of proof tests on silicon nitride that both the maximum flaw size and the presence of a sintering skin and its thickness are decisive factors that influence the life of ceramic samples [40]. The sintering skin is a reaction layer that develops at the surface during sintering; it is generally much weaker than the bulk and contains large flaws [41]. Nevertheless, it has been argued that the mechanism of crack advancement in ceramics is identical under both cyclic and static loading, whereas, cyclic loading conversely acts to diminish shielding in the crack wake [42, 43]; this phenomenon has been modeled by Dauskardt [44] in the form of cycle-dependent frictional degradation effect on grain bridging. It has also been reported that silicon nitride exhibits higher fatigue limit under static* loading compared to that

* Within this context static fatigue describes damage caused by subcritical crack growth under static load.

under cyclic loading [45, 46, 37, 32]. Subcritical crack growth is known to occur under constant load or constant stress-rate load and is influenced by the environmental conditions affecting the loaded material. Various studies on silicon nitride [39, 33, 39] have shown that aqueous environments accelerate subcritical crack growth and thus fatigue compared to air. This effect is attributed to the corrosion of the mechanically stressed crack tips. Through interaction with water molecules, Si-O-Si bonds are broken at the crack tip resulting in weakening the microstructure [47]. On the other hand, high temperatures, especially those above the glass transition temperature, affect subcritical crack growth causing a steep drop in strength [31].

In this study, an experimental program was carried out to characterize a tailored grade of silicon nitride based ceramic as spring material. The fatigue tests were extended to include component tests on ceramic springs in two distinct geometrical configurations. For this purpose bend bars, helical springs and conical disk springs (Belleville washers) were manufactured. The work encompassed cyclic fatigue and constant stress-rate (CSR) tests conducted on bend bars at room temperature and high temperature (1000 °C) as well as in aqueous environment. The influence of three different surface-finish procedures on the fatigue behavior of bend bars was studied in cyclic fatigue tests at room temperature in air atmosphere. Both the helical springs and the disk springs were tested under cyclic fatigue load at 1000 °C. The loads applied in the cyclic fatigue tests were defined by conducting finite element (FE) simulations for the helical springs and analytical numerical calculation for the disk springs to compute the stresses developed in the loaded springs.

2. Methodology and Materials

The investigated silicon nitride ceramic was manufactured from powder (SN-E10 Ube Industries, Ltd., Japan) containing 1.5 wt % Al_2O_3 and 8.1 wt % Y_2O_3 as sintering additives. The powder was gas pressure sintered at 1800 °C under 50 bar nitrogen atmosphere. A density exceeding 99% of the theoretical density was achieved with this sintering process.

Four-point bend bars with dimensions of $3 \times 4 \times 45$ mm^3 were machined according to DIN EN 843-1 [48]. In order to determine the inert strength σ_o, characteristic strength σ_0 and the Weibull modulus m, four-point bending (4PB) tests were performed according to DIN EN 843-1 [48]. Constant stress-rate (CSR) tests were performed on 4PB bars at 20 °C (denoted by RT) and at 1000 °C (denoted by HT) at load rates of 0.04 N/s, 4 N/s and 200 N/s. For each combination of load rate and temperature 30 samples were tested to ensure statistically relevant data. Cyclic fatigue tests were carried out in lab air at 20 °C (RT) and at 1000 °C (HT) and in demineralized water at 20 °C (RT).

Additionally, RT cyclic fatigue tests in air were conducted on samples with different surface-finish procedures: *finish-machined*[†], *white-machined* and *green-machined*. The finish-machined (i.e., ground) samples were ground after sintering, white-machined samples were pre-fired, compressed, ground and then fully sintered, whereas, green-machined samples were ground in the green-body state then fully sintered. This enabled studying the effect of surface finish on the fatigue behavior. The idea behind testing various finishing procedures is to pursue a simpler more cost-effective machining procedure that would deliver comparable results to the standard procedure when finish machining complex ceramic components. The surface roughness of the samples prepared by each procedure was measured by stylus profilometry.

The cyclic load was applied at a frequency of 40 Hz and a load ratio of $R = \sigma_{min}/\sigma_{max} = 0.1$. The tests were stopped after reaching 10^7 cycles. An overview of all tests carried out on bend bars is shown in **Figure 1**.

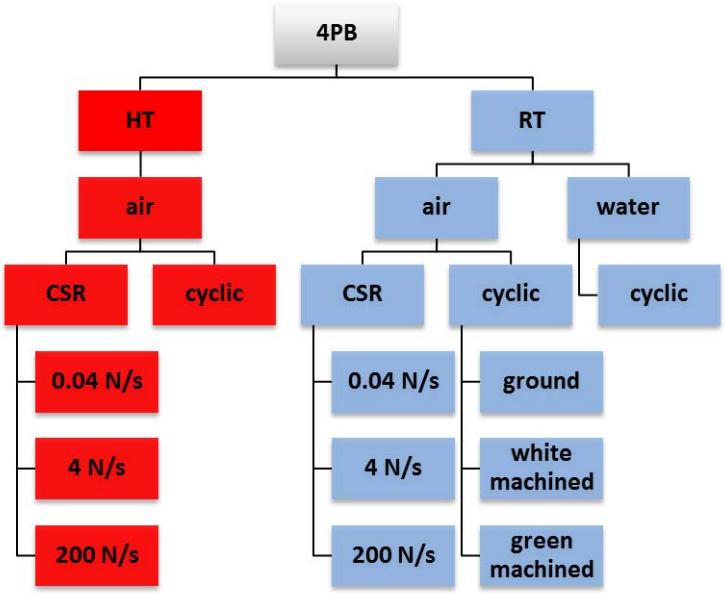

Figure 1. Chart listing the tests carried out on bend bars in a four-point bending configuration.

Indentation tests in accordance with DIN EN 843-4 [49] were conducted to determine the hardness and indentation fracture (IF) toughness. The elastic modulus as function of temperature was measured up to 800 °C in 4PB in accordance with DIN EN 843-2 [50]. Using the resonance method, the stiffness of the samples was measured up to 1200 °C and normalized to its value at RT (i.e., the RT stiffness was set to 1.0). By fitting the 4PB data to the stiffness data obtained from the resonance method, the elastic modulus was predicted in the temperature range between 800 °C and 1200 °C.

[†] All bend bars tested throughout this work were finish-machined (i.e., ground) samples unless explicitly stated otherwise.

Additionally, compression helical springs with a rectangular "wire"[‡] section and flat-ground ends (Figure **2a**) were fabricated. The same procedure for green-body pressing of the bend bars was applied to the helical springs. Prior to sintering, the outer diameter and the side faces were created by turning the green bodies on a lathe and subsequently milling the rectangular wire section of the springs. Due to the complexity of the geometry, it was not possible to mill a round section. A subsequent gas pressure sintering process enabled producing high-strength parts, from which the springs with tight dimensional tolerances and very good surface quality were produced by grinding and surface finishing.

Conical disk springs (Belleville washers) (**Figure 2b**) were also fabricated for high-temperature cyclic fatigue testing and characterization. Similar to the helical springs, the pressing of the green bodies was identical to that of the bend bars. Subsequently, the parts were isostatically pressed at 150 MPa, machined, and after sintering the entire surface of each part was finish-machined.

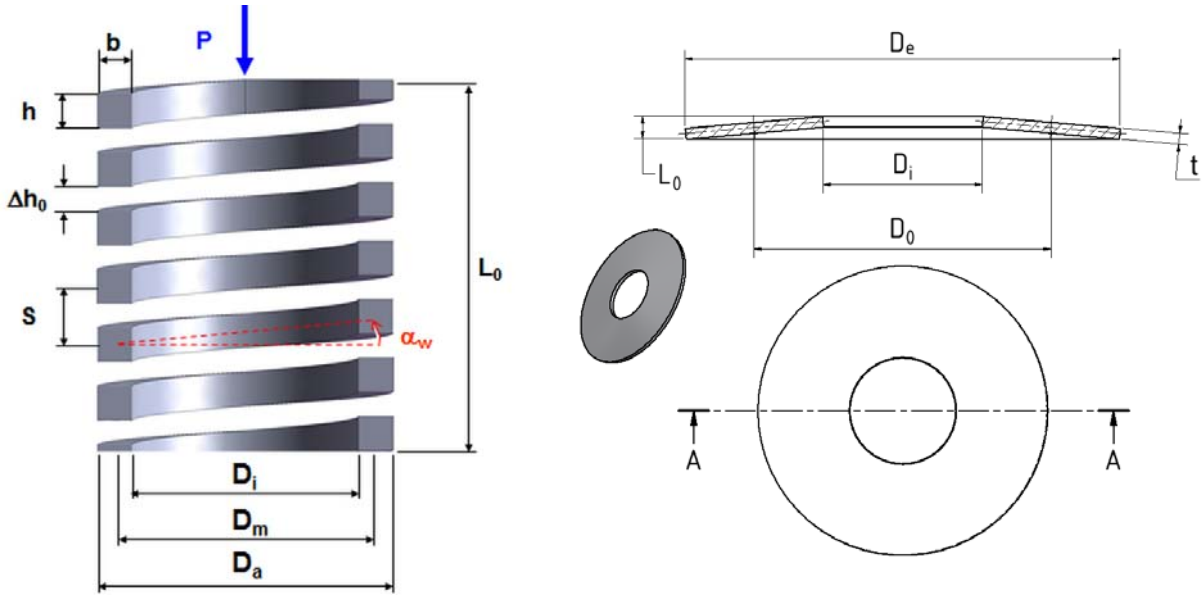

(a) (b)

Figure 2. Schematic drawing showing the dimensions of the (a) helical springs: D_a=10.000 mm, D_i=7.274 mm, b=1.363 mm, h=2.608 mm, s=3.608 mm, L_0=13.000 mm, number of active coils n_f=2.880, Δh_0=1.0 mm (redundant value), α_w: coil angle (redundant), and the (b) disk springs: D_e=50.12 mm, D_i=18.4 mm, L_0=2.62 mm, t=1.25 mm.

The cyclic fatigue tests on both the helical springs and the disk springs (setup shown in **Figure 3)** were carried out at 1000 °C, a frequency of 20 Hz and a load ratio of $R = \sigma_{min}/\sigma_{max} = 0.1$. Here it should be noted that the load ratio (R) in component testing was calculated based on the peak value of the maximum principal stress in the component for two reasons: (i) ceramics are more sensitive to tensile

[‡] Although the term "wire" is generally reserved for metals it will be used within this context to indicate the machined section of the helical springs.

stresses than compressive stresses and (ii) loading components, such as springs, results in a triaxial stress state. As will be detailed in Section 3, the load applied in the fatigue tests was determined by calculating the stresses in the springs. The tests were stopped after reaching 10^7 cycles. Samples fractured prior to 100 cycles were discarded from the analysis.

(a) (b)

Figure 3. Cyclic fatigue test setup for (a) helical compression springs and (b) disk springs.

CSR tests on bend bars enable the evaluation of subcritical crack growth parameters based on the power equation [51]

$$v = CK_I^p = C^*\left(\frac{K_I}{K_{Ic}}\right)^p \quad (1)$$

where v is the crack velocity ($v = da/dt$; a is the crack length, t is the time), C is a constants dependent on the material and the environment, K_I is the stress intensity factor, K_{Ic} is the fracture toughness and p is the subcritical crack growth exponent. The value of p can be evaluated from the slope of the strength σ_f vs. stress rate $\dot{\sigma}$ diagram as follows [51]

$$\log \sigma_f = \frac{1}{p+1}\log \dot{\sigma} + \frac{1}{p+1}\log\left((p+1)D\sigma_c^{p-2}\right) \quad (2)$$

where D *is a* material parameter and σ_c is the inert strength. To obtain the values of p and D, the inert strength of the material (σ_c) must be determined in advance.

The cyclic crack-growth rate (da/dN) in ceramics, where N is the number of load cycles, can be described by a Paris-law expression in terms of the applied stress intensity range ΔK_I and the fracture toughness K_{IC}, in addition to two parameters, namely, a material parameter A and the crack-growth exponent n [52]:

$$\frac{da}{dN} = A(\Delta K_I)^n = A^* \left(\frac{\Delta K_I}{K_{Ic}}\right)^n \quad (3)$$

and hence, the stress range $\Delta\sigma$ can be given in terms of the number of cycles to failure (N_f) as follows:

$$\log \Delta\sigma = \frac{1}{n}\log(B\sigma_c^{n-2}) - \frac{1}{n}\log N_f \quad (4)$$

from which $-1/n$ is the slope of the $\log \Delta\sigma$ vs. $\log N_f$ plot.

The relation between the number of cycles to failure (N_f) and the stress amplitude (or the stress range $\Delta\sigma$) can be obtained from the crack growth rate relation by integration from the initial crack size (a_i) to the critical crack size (a_c). Assuming that the lifetime and strength under both static and cyclic loading are both caused by the same flaw population, the following equation applies [52]:

$$N_f = \frac{B\sigma_c^{n-2}}{(\Delta\sigma)^n} = \frac{B\sigma_c^{n-2}}{\sigma_{max}^n(1-R)^n} \quad (5)$$

given that

$$B = \frac{2K_{Ic}^{2-n}}{AY^2(n-2)} = \frac{2K_{Ic}^2}{A^*Y^2(n-2)} \quad (6)$$

where Y is the crack shape factor. In line with [51], a value of $Y = 1.3$ may be safely assumed for the calculation of B.

3. Failure probability and stresses in ceramic springs

3.1. Failure probability

The failure probability of an applied stress distribution over the whole component volume (V) in static loading is given by [51]

$$F = 1 - \exp\left(-\int_V \frac{1}{V_0}\left(\frac{\sigma(x,y,z)}{\sigma^*}\right)^m dV\right) \quad (7)$$

where V_0 is the scaling volume, m is the Weibull modulus and σ^* is the Weibull material scale parameter. By defining the stress distribution in the component such that

$$\sigma(x,y,z) = \sigma f(x,y,z) \quad (8)$$

where *f(x,y,z)* is a distribution function and σ is a load-dependent stress magnitude at a point (for ceramics this value is equal to the maximum principal stress), one may define an effective volume of the component ($V_{eff,comp}$) which is given by

$$V_{eff,comp} = \int_V f(x,y,z)^m dV \tag{9}$$

Hence, **Eq.(7)** may be written as follows [53]

$$F = 1 - \exp\left(-\frac{V_{eff,comp}}{V_0}\left(\frac{\sigma}{\sigma^*}\right)^m\right) \tag{10}$$

By relying on strength data obtained from the CSR tests on bend bars, the Weibull material scale parameter (σ^*) may be expressed in terms of the effective volume of the 4PB sample ($V_{eff,4PB}$) normalized to the scaling volume (V_0) and the characteristic Weibull strength ($\sigma_{0,4PB}$) obtained from the same tests such that

$$\sigma^* = \left(\frac{V_{eff,4PB}}{V_0}\right)^{1/m} \sigma_{0,4PB} \tag{11}$$

wherein for simplicity the characteristic strength ($\sigma_{0,4PB}$) will be denoted by σ_0 so that

$$\sigma^* = \left(\frac{V_{eff,4PB}}{V_0}\right)^{1/m} \sigma_0 \tag{12}$$

and hence, the failure probability of the component becomes

$$F = 1 - \exp\left(-\frac{V_{eff,comp}}{V_{eff,4PB}}\left(\frac{\sigma}{\sigma_0}\right)^m\right) \tag{13}$$

where the component strength ($\sigma_{0,comp}$) is given by

$$\sigma_{0,comp} = \sigma_0 \left(\frac{V_{eff,4PB}}{V_{eff,comp}}\right)^{1/m} \tag{14}$$

The effective volume of bend bars loaded in four-point bending may be calculated, after ignoring shear stresses between the load points and the supports, according to the form given in [53]

$$V_{eff,4PB} = \left[\left(\frac{L_i}{L_0}\right)m + 1\right]\left[\frac{1}{2(m+1)^2}\right]V_B, \qquad V_B = bhL_0 \tag{15}$$

where in this particular case L_i = 20 mm is the span between the load points, L_0 = 40 mm is the span between the supports, h = 3 mm and b = 4 mm are the height and breadth of the bend bard, respectively, and m is the Weibull modulus.

In the case of cyclic loading, the failure probability is given by [51]

$$F = 1 - \exp\left(-\left(\frac{V_{eff,comp}}{V_{eff,4PB}}\right)^{m^*/m}\left(\frac{N_f}{N_0}\right)^{m^*}\right) \tag{16}$$

where

$$m^* = \frac{m}{n-2} \tag{17}$$

and

$$N_0 = \frac{B\sigma_0^{n-2}}{(\Delta\sigma)^n} = \frac{B\sigma_0^{n-2}}{\sigma_{max}(1-R)^n} \tag{18}$$

where the values for B and n are obtained from evaluating fatigue data (refer to **Eq.(4))**, σ_{max} is the maximum stress in the component, $R = \sigma_{min}/\sigma_{max}$ is the load ratio and the values for m and σ_0 are obtained from 4PB strength data under static loading.

3.2. Stress computations

The stress state in both the helical springs and the disk springs was computed to determine the corresponding load limits for the fatigue experiments. Finite element (FE) simulations were carried out for the helical springs whereas, computations based on analytical formulas were used for the disk springs.

3.2.1. Helical springs

The spring deflection f (defined as the difference between the free length L_0 and the loaded height) can be calculated according to [54]

$$f = \frac{\varphi D_m^3 n_f}{b^2 h^2 G} P \tag{19}$$

where b is the wire section width (side of the cross section perpendicular to the axis of the spring), h is the wire section height (side of the cross section parallel to the axis of the spring), D_m is the mean coil diameter, n_f is the number of active coils, φ is the stiffness coefficient dependent on the ratio b/h or h/b

(whichever is ≥ 1.0 depending on the type of coiling), *G* is the shear modulus and *P* is the spring load. The maximum shear stress may be calculated according to [54]

$$\tau_{max} = \frac{\zeta D_m}{bh\sqrt{bh}} P \qquad (20)$$

where ζ is the stress coefficient dependent on the ratio *b/h* or *h/b* (whichever is ≥ 1.0 depending on the type of coiling).

Unlike in steel springs, the spring deflection and the maximum shear stress given by **Eq. (19)** and **Eq. (20)** prove to be insufficient design criteria for ceramic springs. This is particularly true since **Eq. (20)** does not contain any information on the load distribution over the wire cross section and since, unlike in metals, the maximum shear stress is not particularly the suitable critical quantity required for predicting failure of brittle materials, which is better assessed by relying on the maximum tensile stress. Moreover, the application of both equations may also be subject to uncertainties due to the method, by which both coefficients φ and ζ are evaluated. This is attributed to the fact that spring design information found in standards is exclusively meant for metallic materials that undergo plastic deformation. Ceramics, on the other hand, do not exhibit the same strength tolerance once the maximum load has been exceeded. Hence, a finite element simulation model is more adequate to calculate the stresses and strains undergone by the loaded spring.

A set of various three-dimensional finite element (FE) models were developed in COMSOL and ANSYS with different levels of complexities ranging from repeating geometrical units, i.e., modeling a single coil to obtain the spring elasticity characteristics and the stress distribution across the wire section (**Figure 4a**), up to a fully detailed model of a spring to study stress concentrations at the spring ends (**Figure 4b**).

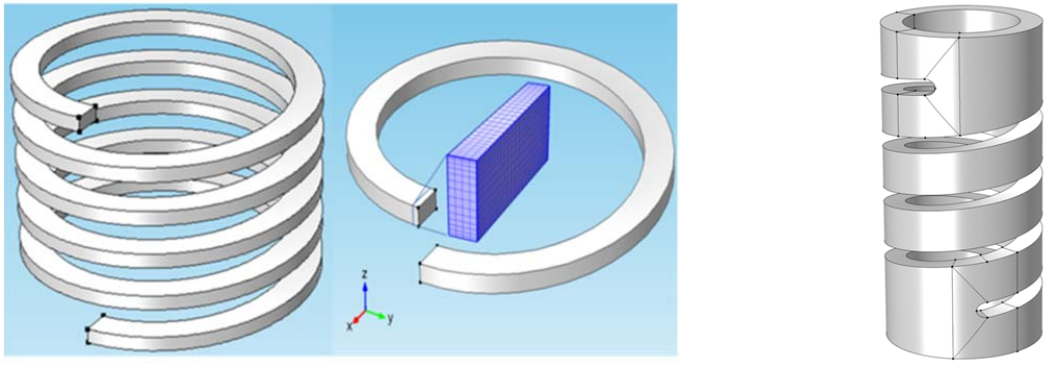

(a) (b)

Figure 4. Finite element simulation models of the helical spring (a) single coil model, (b) full spring model.

Initially, a parametric study was carried out in COMSOL with a single coil (repeating unit) model to optimize the geometrical design parameters of the helical spring; the design criterion was set to achieve a failure probability below 0.0001% at a given applied load. This automated procedure, whose details may be found in [55], was carried out using the single coil model to calculate the coefficients φ and ζ (refer to Eq.(19) and Eq.(20)) as well as the effective volume ($V_{eff,comp}$) needed in Eq. (14). After running approx. 12,000 simulations, this optimization procedure enabled generating a database which was subsequently used as input data for a post-processing procedure in a computer code for dimensioning the wire cross section. After selecting potential design variants, a full spring FE model was created and run in ANSYS. The final dimensions of the helical springs used in this study are listed in **Table 1**.

Table 1. Dimensions of the helical springs (refer to Figure **2a**).

D_a [mm]	D_i [mm]	b [mm]	h [mm]	s [mm]	L_0 [mm]	n_f [-]	Δh_0 [mm]
10.000	7.274	1.363	2.608	3.608	13.000	2.880	1.0

The load was applied by setting a spring deflection; the corresponding spring force is obtained from the analysis as a dependent variable. In this particular case the spring deflection was set to f = 0.9 mm, which yields a spring force of P = 85 N.

In addition to the maximum principal stress, which gives the maximum tension in the component, the effective volume was also determined; both of which are required for the calculation of the failure probability.

3.2.2. Disk springs

An analytical solution based on a truncated conical shell and detailed by Kobelev [56, 57] was applied to calculate the stresses developing in a loaded disk spring. Figure **5a** shows the truncated conical shell in its undeformed state; it has a thickness t, slope angle α (constant) and inner and outer radii of the middle surface denoted by r_a, and r_b, respectively, with their ratio being $\Delta = r_b / r_a$. The deformed state of the spring is shown in Figure **5b**.

The middle surface of an unloaded spring is thus, described by the parametric equations

$$r = c - x\cos\alpha$$
$$z = -x\sin\alpha \qquad (21)$$

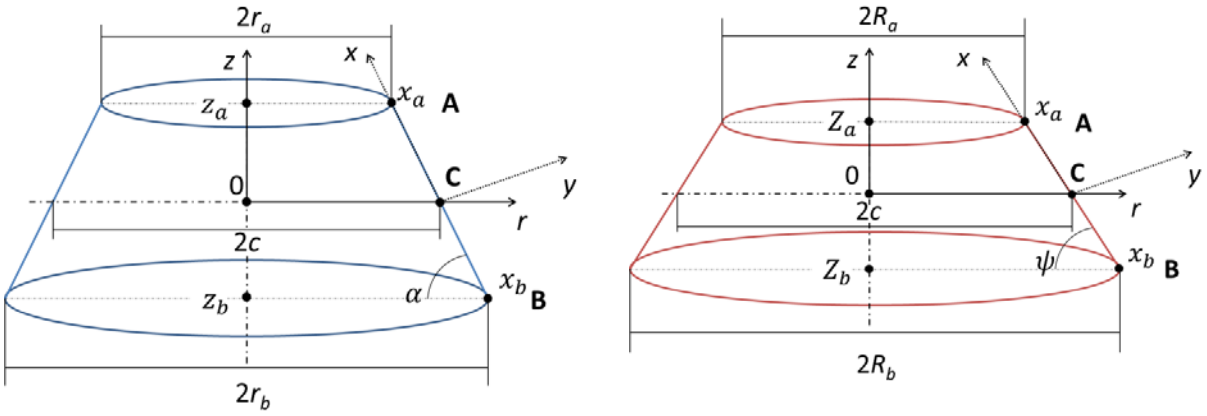

(a) (b)

Figure 5. Middle-surface representation of an (a) unloaded, (b) loaded truncated conical shell **[57]**.

where in a cylindrical coordinate system (r,z,θ) the radius (r) is bound by $r_a \leq r \leq r_b$ and the height (z) is bound by $z_b \leq z \leq z_a$ (where $z_a > 0$ and $z_b < 0$) so that

$$\begin{aligned} r_a &= c - x_a \cos\alpha, \\ r_b &= c - x_b \cos\alpha, \\ z_a &= x_a \sin\alpha, \\ z_b &= x_b \sin\alpha \end{aligned} \tag{22}$$

A point on the middle surface with the coordinates (x,Y,θ) has the arc length x, measured from point **C**, which is bound by $x_b \leq x \leq x_a$ (where $x_a > 0$ and $x_b < 0$), and the coordinate y, which represents the normal distance from the point to the middle surface of the shell and is bound by $-t/2 \leq y \leq t/2$.

The principal radii of curvature r_1 and r_2 of the middle surface for an unloaded conical shell are given by

$$\begin{aligned} \frac{1}{r_1} &= \frac{\sin\alpha}{r}, \\ \frac{1}{r_2} &= 0 \end{aligned} \tag{23}$$

In its deformed state, see Figure **5b**, the slope angle (ψ) is also constant along the meridian and the middle surface of the loaded spring may be described by the parametric equations

$$\begin{aligned} R &= c - x\cos\psi \\ Z &= -x\sin\psi \end{aligned} \tag{24}$$

where the radius (R) is bound by $R \leq R \leq R_b$ and the height (Z) is bound by $Z_b \leq Z \leq Z_a$ so that

$$
\begin{aligned}
R_a &= c - x_a \cos\psi, \\
R_b &= c - x_b \cos\psi, \\
Z_a &= x_a \sin\psi, \\
Z_b &= x_b \sin\psi,
\end{aligned}
\tag{25}
$$

The radius of the inversion center point **C** (refer to **Figure 5**), i.e., the value of c in Eq. (24) and Eq. (25), may be found by applying the condition of vanishing circumferential forces, which yields

$$
c = \frac{\Delta - 1}{\ln \Delta} r_a \tag{26}
$$

The principal radii of curvature R_1 and R_2 of the middle surface for a loaded conical shell are given by

$$
\begin{aligned}
\frac{1}{R_1} &= \frac{\sin\psi}{r}, \\
\frac{1}{R_2} &= 0
\end{aligned}
\tag{27}
$$

The circumferential stress (σ_1), meridional stress (σ_2) and normal stress (σ_3) are given by [58]

$$
\begin{aligned}
\sigma_1 &= \frac{E}{(1+\nu)(1-2\nu)}[(1-\nu)\varepsilon_1 + \nu(\varepsilon_2 + \varepsilon_3)] \\
\sigma_2 &= \frac{E}{(1+\nu)(1-2\nu)}[(1-\nu)\varepsilon_2 + \nu(\varepsilon_3 + \varepsilon_1)] \\
\sigma_3 &= \frac{E}{(1+\nu)(1-2\nu)}[(1-\nu)\varepsilon_3 + \nu(\varepsilon_1 + \varepsilon_2)]
\end{aligned}
\tag{28}
$$

where ε_1, ε_2 and ε_3 are the circumferential, meridional, and normal strains, respectively.

Symmetry conditions result in zero shear strains and stresses and thus, in the absence of radial deformation, the stresses in the meridional (σ_2) and normal (σ_3) directions may be assumed zero. Hence, both the meridional strain (ε_2) and the normal strain (ε_3) become identical and a function of the circumferential strain (ε_1)

$$
\begin{aligned}
\varepsilon_2 &= -\nu\varepsilon_1 \\
\varepsilon_3 &= -\nu\varepsilon_1
\end{aligned}
\tag{29}
$$

and

$$
\begin{aligned}
&\varepsilon_1 = \epsilon_1 + y\kappa_1 \\
&= \frac{(\cos\alpha - \cos\psi)x + (\sin\psi - \sin\alpha)y}{c - x\cos\alpha}
\end{aligned}
\tag{30}
$$

where ϵ_1 is the circumferential mid-surface strain [58] and κ_1 is the circumferential curvature [59] given by

$$\epsilon_1 = \frac{R-r}{r} = \frac{\cos\alpha - \cos\psi}{c - x\cos\alpha}x$$
$$\kappa_1 = \frac{1}{R_1} - \frac{1}{r_1} = \frac{\sin\psi - \sin\alpha}{r} \quad (31)$$

For the calculation of the failure probability for an applied stress distribution, Eq. (10) may be written in the form

$$F = 1 - \exp\left(-\left(\frac{\sigma_{max}}{\sigma^*}\right)^m \int_V \left(\frac{\sigma(x,y,z)}{\sigma_{max}}\right)^m dV\right) \quad (32)$$

where σ_{max} is the maximum stress in the component and $\sigma(x,y,z)$ denotes the applied stress at each point; hence, the effective volume can be calculated by evaluating the integration

$$V_{eff} = \int_V \left(\frac{\sigma(x,y,z)}{\sigma_{max}}\right)^m dV \quad (33)$$

which delivers the effective volume in terms of the geometry of the component and the applied stress normalized to its maximum value in the component.

The elastic constants used in the computations were: elastic modulus E = 295 GPa and Poisson's ratio ν = 0.3. A code was programmed in Matlab to calculate the stresses across the spring wall thickness as function of the slope angle (ψ) and to perform the numerical integration given in Eq. (33) to calculate the effect volume of the disk spring. The spring force needed for the fatigue tests was calculated in accordance with DIN EN 16984 [60].

4. Results

4.1. Hardness, fracture toughness, and elastic modulus

Using six different samples each tested five times, the room-temperature Vickers hardness was found to be HV10 1412.2±23.9, which corresponds to a value of 14.9±0.3 GPa. The indentation fracture toughness was measured to be K_{IC} = 5.6±0.3 MPa.m$^{1/2}$.

The elastic modulus was measured in 4PB up to 800 °C. Its values between 800 °C and 1200 °C were then obtained by fitting the data to the normalized stiffness measurements obtained from the resonance method; **Figure 6**. The values show a decline in stiffness beyond 800 °C and a steeper slope beyond 1000 °C.

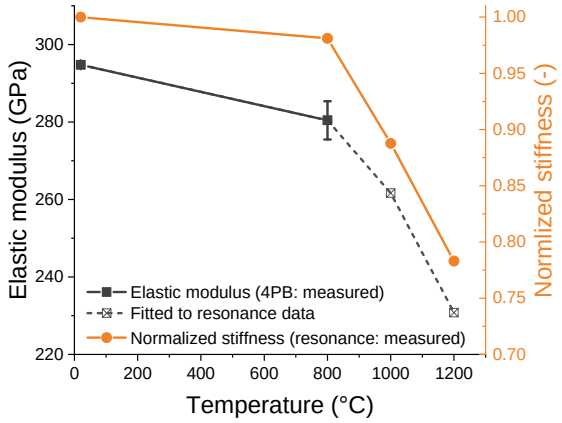

Figure 6. Elastic modulus as function of temperature

4.2.Static loading (CSR tests)

The strength σ_f vs. load rate $\dot{F}$ (0.04 N/s, 4 N/s and 200 N/s) and strength σ_f vs. stress rate $\dot{\sigma}$ plots obtained from static 4PB tests in lab air data are shown in **Figure 7a** and **b**, respectively.

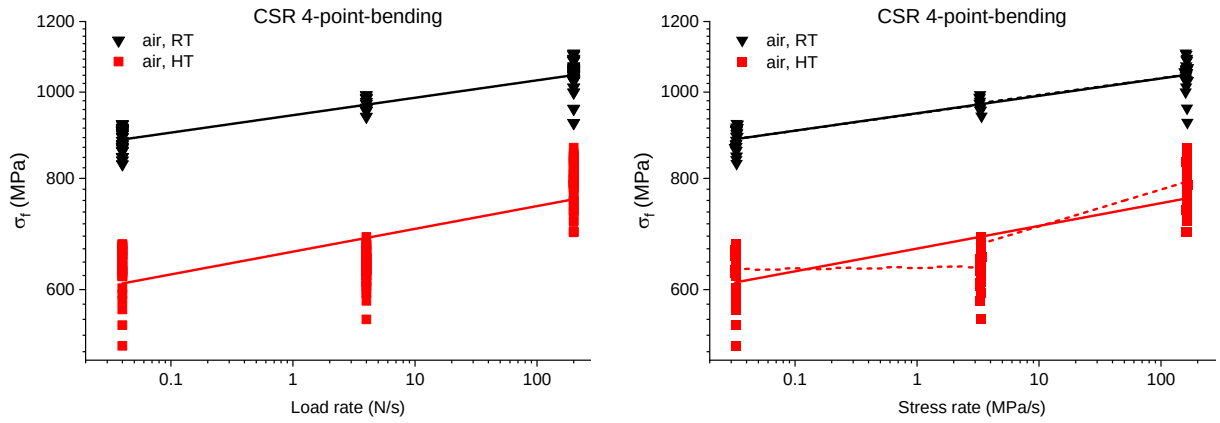

(a) (b)

Figure 7. CSR data from 4PB tests shown in logarithmic scale (a) strength vs. load rate, (b) strength vs. stress rate.

A Weibull diagram ($\ln\ln(1/(1-F))$ vs. $\ln\sigma$), where *F* is the failure probability, for different load rates at RT and HT is shown in **Figure 8**.

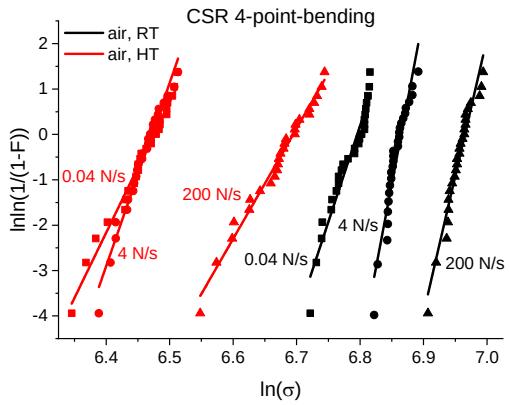

Figure 8. Weibull diagram from 4PB tests for different load rates at RT and 1000 °C.

Table 2 lists the mean strength in 4-point-bending ($\bar{\sigma}_{4PB}$), the characteristic strength (σ_0) and the Weibull modulus (m) obtained for each load case.

Table 2. Strength and Weibull parameters obtained from the CSR 4PB tests.

	Load rate [N/s]	**0.04**	**4**	**200**
air, RT	$\bar{\sigma}_{4PB}$ [MPa]	885.0 ± 25.6*	966.9 ± 16.3	1045.7 ± 36.9
	σ_0 [MPa]	896.9	974.9	**1063.3**
	m [-]	41.1	66.5	**32.9**
air, HT	$\bar{\sigma}_{4PB}$ [MPa]	632.5 ± 37.7	636.3 ± 27.7	792.2 ± 44.9
	σ_0 [MPa]	650.0	648.8	**812.5**
	m [-]	19.4	27.6	**21.1**

*Standard deviation

Based on the form presented in **Eq. (15),** the effective volume of the 4PB bars is $V_{eff,4PB} \cong 5.68$ mm^3. The results of the HT tests indicate almost similar characteristic strength values for the two lower load rates (0.04 N/s and 4 N/s) and a significantly higher strength at 200 N/s. The RT data showed an almost steady increase in strength with increasing load rate. Moreover, the σ_f vs. $\dot{\sigma}$ graphs did not reveal a plateau in the slope, from which inert strength may be calculated; hence, the inert strength may be obtained from the highest stress rate curves. Accordingly, the inert strength σ_c of this material is 1063.3 MPa and 812.5 MPa at 20 °C and 1000 °C, respectively.

Based on the inert strength values calculated from the Weibull diagrams at the highest load rates, subcritical crack growth parameters *p* and *D* were calculated according to **Eq. (2)**; the values are listed in **Table 3**.

Table 3. Subcritical crack growth (SCG) parameters according to **Eq. (2)**.

	p **[-]**		***D*** **[MPa^2·s]**	
air, RT	50.1		5.78×10^4	
air, HT	38.2		5.45×10^3	
	p **[-]**		***D*** **[MPa^2·s]**	
	0.04 to 4 [N/s]	**4 to 200 [N/s]**	**0.04 to 4 [N/s]**	**4 to 200 [N/s]**
air, RT	50.9	52.1	5.0×10^4	5.4×10^4
air, HT	665.8	23.1	-	7.09×10^4

A lower value of *p* indicates higher sensitivity of strength to change in stress at high temperature. However, it is obvious from the data in **Table 3** that the HT tests show different slopes between 0.04 N/s - 4 N/s and 4 N/s - 200 N/s, and hence, calculating *p* between each two load rates would be necessary. For the HT tests, *p* was found to be 665.7 and 23.1 between 0.04 N/s and 4 N/s and between 4 N/s and 200 N/s, respectively. The high *p* value in the first portion of the σ_f vs. $\dot{\sigma}$ graph (i.e., 0.04 N/s - 4 N/s) indicates almost no strength sensitivity to variation in stress. On the contrary, the RT data (**Table 3**) shows very close values for *p* and *D* in both segments of the curve (i.e., between 0.04 N/s - 4 N/s and 4 N/s - 200 N/s) compared to their values when calculated for the whole range of stress rates.

4.3. Stresses in the helical springs

By applying a spring deflecting of 0.9 mm, the FE simulation showed a maximum principal stress value of 376 MPa in the whole spring; the peak value in the wire cross section amounted to 356 MPa, see **Figure 9**. Given the proportionality in the stress-strain relationship in the helical springs, a constant effective volume may be obtained. By post-processing the FE simulation results and based on the values σ_0 = 812.5, m = 21.1 (refer to Table 2) and $V_{eff,4PB}$ = 5.68 mm^3, the effective volume was found to be $V_{eff,helical}$=0.23 mm^3. By applying Eq. (14), the value of the critical stress adjusted for the effective volume was found to be $\sigma_{0,helical}$ = 945.8 MPa.

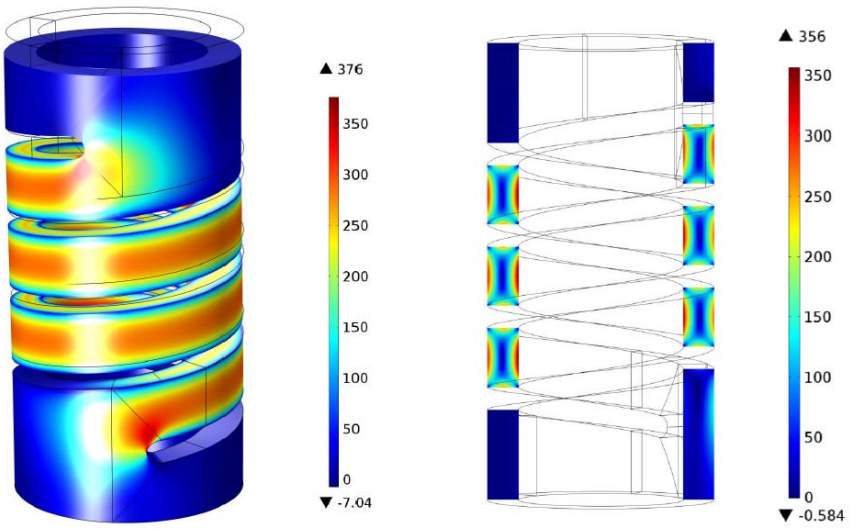

Figure 9. Maximum principal stress distribution in the (left) whole spring, (right) wire cross section.

To obtain a load ratio R = 0.1 in the fatigue tests, the minimum and maximum loads were set at F_{min} = 7 N and F_{max} = 70 N; it should be again noted that force-stress relationship is proportional.

4.4. Stresses in the disk springs

The analytical model detailed in Section 3.2.2 was used to calculate the stresses as function of the slope angle in its deformed state (ψ). The circumferential stress (maximum tensile stress) was calculated throughout the wall thickness of the spring, from which a lower and upper bound for the spring force were determined to run the fatigue tests at a load ratio of R=0.1. The fatigue tests on the disk springs were carried out at an upper maximum stress of 400 MPa; hence, the lower and upper spring forces were calculated to be around 105 N and 930 N, respectively.

Unlike helical springs, the stress-strain relationship in disk springs is nonlinear, and thus, the effective volume becomes dependent on the applied load. The effective volume was calculated by performing numerical integration of Eq. (33) in Matlab based on the following parameters: σ_0 = 812.5, m = 21.1 (refer to Table 2) and $V_{eff,4PB}$ = 5.68 mm^3. By applying Eq. (14) through an iterative procedure, the critical stress adjusted for the effective volume was found to be $\sigma_{0,disk}$ = 759.4 MPa at an angle of ψ = 1.766°, whereas the effective volume was calculated to be $V_{eff,disk}$=23.60 mm^3. **Figure 10** shows the circumferential stress distribution throughout the wall thickness under this specific load; the maximum tensile stress appears at the lower edge of the outer surface of the spring, i.e., at coordinates ($x = x_b$, $y = -t/2$).

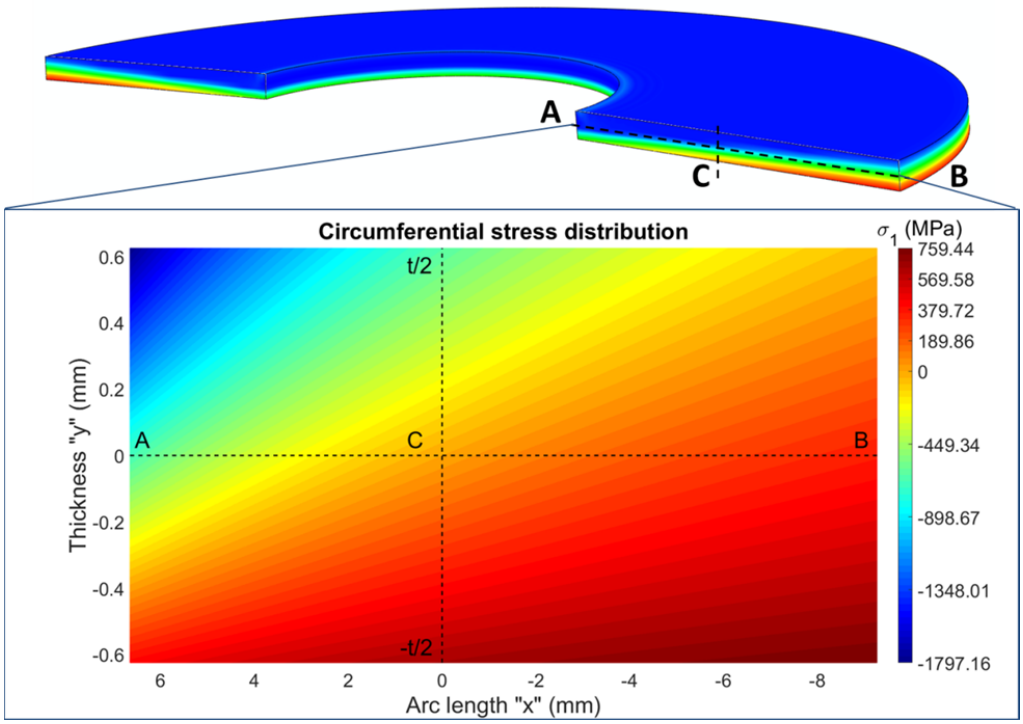

Figure 10. Circumferential stress distribution across the wall thickness of the disk spring $\psi = 1.766°$ (dimensions given in **Figure 2b**); points **A**, **B** and **C** lie on the middle surface.

The computation was carried out for an undeformed slope angle of $\alpha = 4.937°$ and a deformed angle of $\psi = 1.766°$, which corresponds to a spring deflection of $f = 0.88$ mm and an applied normal load of around $F_N = 1595$ N.

4.5. Cyclic fatigue

The cyclic 4PB test results are shown in **Figure 11** as *S-N* curves by plotting the stress range ($\Delta\sigma = 2\sigma_a$; where σ_a is the stress amplitude) against the number of cycles until failure (N_f) on a logarithmic scale.

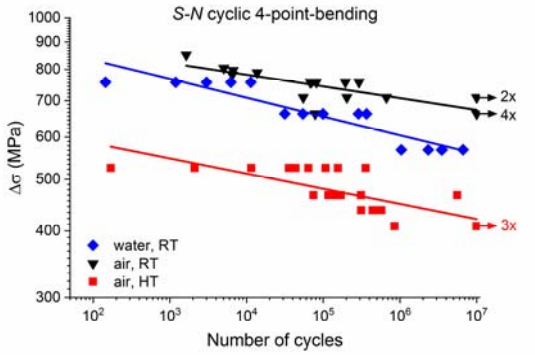

Figure 11. *S-N* curves from cyclic fatigue tests on bend bars in 4PB at RT and 1000 °C.

The *S-N* curves indicate the lowest fatigue strength for the HT tests followed by RT in water and the highest for RT in lab air.

The *S-N* curves from the HT cyclic fatigue tests conducted on bend bars, helical springs and disk springs are shown in **Figure 12a**. For the helical springs, any sample failed before reaching 100 cycles was plotted at $N=10^0$ and discarded when calculating the regression equation. By normalizing the stress range to the critical stress obtained from Eq. (14), effective-volume-adjusted *S-N* curves were constructed as shown in **Figure 12b**.

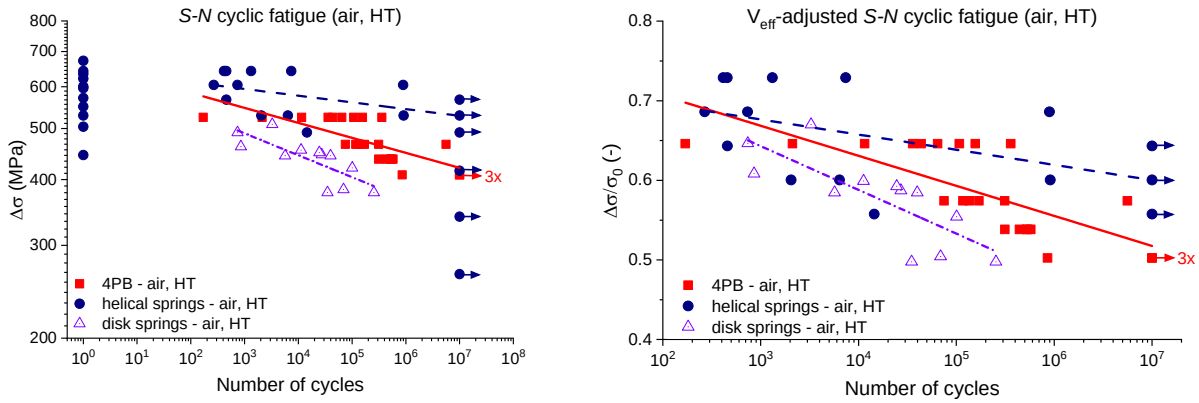

(a) (b)

Figure 12. Cyclic fatigue (a) *S-N* data, (b) effective-volume-adjusted *S-N* data; T=1000 °C.

The critical stress for the bend bars was found from the CSR tests to be σ_0 = 812.5 MPa (refer to Table 2), whereas, the critical stress for the helical springs and the disk spring were calculated to be around $\sigma_{0,helical}$ = 945.8 MPa and $\sigma_{0,disk}$ = 759.4 MPa, respectively.

Crack propagation rate curves (*da/dN* vs. $\Delta K/K_{IC}$) were constructed in accordance with the procedure detailed in Fett et al. [61] and Härtelt et al. [62], **Figure 13.** The value of K_{IC} was set to 6.5 MPa.m$^{1/2}$ and assuming surface cracks, the crack form factor needed for the evaluation of the propagation rate (*da/dN)* was assumed to be Y = 1.3 [61]. For the helical springs, any sample plotted at $N=10^0$ in addition to the the three run-outs recorded at the lowest stress levels (i.e., $\Delta\sigma$= 264.6 MPa, $\Delta\sigma$= 340.2 and $\Delta\sigma$= 415.8) were discarded from the statistical analysis. The crack-growth parameters of **Eq. (3)** for cyclic loading were calculated and listed in **Table 4**.

Table 4. Crack growth parameters for the cyclic fatigue tests according to **Eq. (3)**.

	n **[-]**	***A**** **[m/cycle]**
4PB bars, air, HT	16.0	4.8×10^{-8}
Helical springs, air, HT	22.0	6.7×10^{-8}
Disk springs, air, HT	11.9	2.7×10^{-7}

From the cyclic fatigue data presented in **Figure 12**, **Figure 13**, and **Table 4** the highest crack propagation rate appears to be in helical springs, followed by the 4PB bars and the lowest for the disk springs. On the other hand, the *S-N* curves indicate the highest fatigue strength for the helical springs and the lowest for the disk springs.

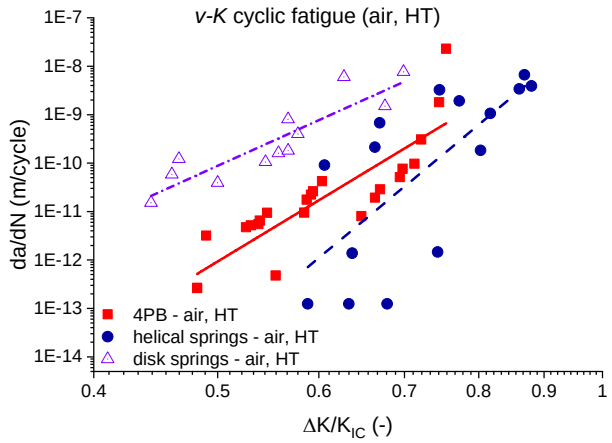

Figure 13. Crack propagation rate curves (*v-K)* obtained from HT tests on bend bars in 4PB, helical springs and disk springs.

A fractographic analysis was carried out by inspecting the fracture surfaces of selected bend bars under the light microscope and the SEM (**Figure 14**). Of particular interest were the samples that exhibited low strength or underwent a small number of cycles to failure. The fractographic analysis revealed that the fracture origin appeared in almost all cases on the tensile side of the bend bars; in some cases the fracture origins were near-surface material defects such as inclusion, pores or large grains. Transgranular fracture was predominant at RT both in air and water (**Figure 14a** and **c**). The inspected fracture surfaces of the samples tested at HT pointed out to intergranular fracture and glassy phase residues on the grains; **Figure 14b**. No corrosion-induced microstructural alterations were detected in the tests carried out under water; **Figure 14c**. The presence of fractured grains and fracture debris was confirmed by the analysis.

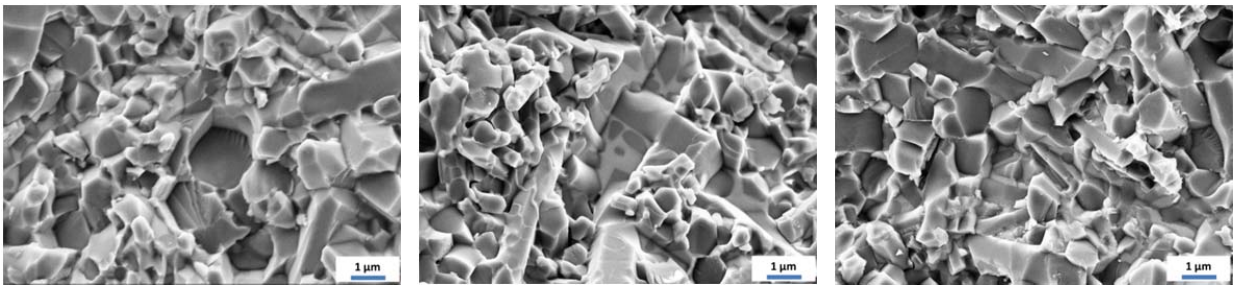

(a) (b) (c)

Figure 14. SEM images showing the fracture surfaces of bend bars tested in 4PB cyclic fatigue (a) in air at RT, (b) in air at 1000 °C and (c) in water at RT.

Surface inspection and fractographic analysis were conducted on samples of both types of springs; the surface morphology and fracture patterns are shown in **Figure 15**. Determining the fracture origin in helical springs turned out to be a challenging endeavor given the irregular fracture pattern. Fracture origins in disk springs were possible to locate in some samples at the lower outer edge of the spring. Rougher surface morphology was noticed when comparing the fracture surfaces of helical springs with those of disk springs. Similar to the bend bars tested at HT (**Figure 14b**) but to a lesser extent, the fracture surfaces of both helical and disk springs showed intergranular fracture.

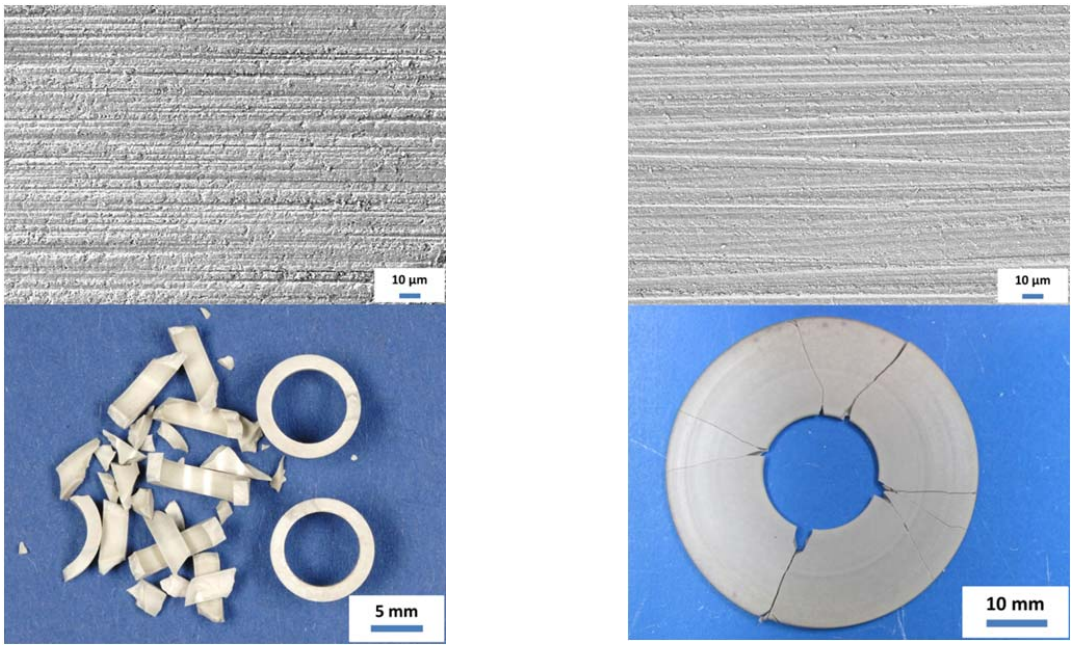

(a) (b)

Figure 15. Surface morphology and fracture pattern of (a) helical springs and (b) disk springs tested in cyclic fatigue at 1000 °C.

4.6. Effect of surface-finish procedure on cyclic fatigue

Three surface-finish procedures were investigated resulting in finish-machined, white-machined and green-machined samples. The surface morphology of the three grades was inspected under the SEM as shown in Figure **16**.

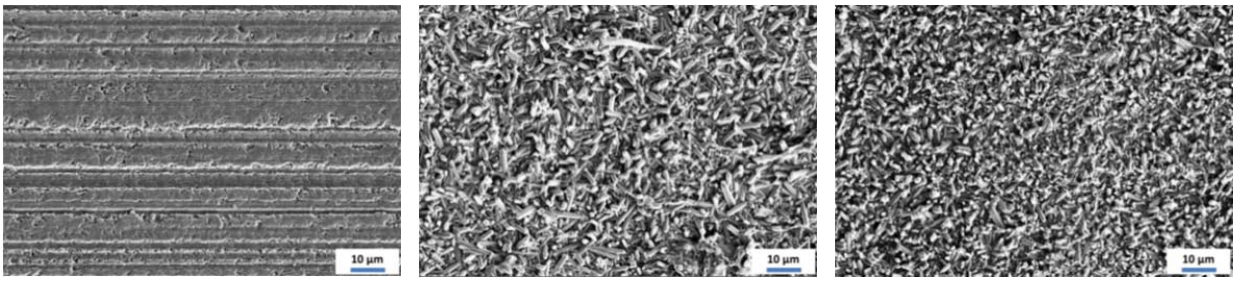

(a) (b) (c)

Figure 16. SEM images showing the surface morphology of (a) finished-machined, (b) white-machined, and (c) green-machined samples.

Given the three different finishing procedures, only finish-machined samples show grinding striations on the surface, unlike both white and green-machined, which underwent sintering as a final fabrication step. The surface roughness (measured against the grinding direction) of the three types of samples is given in Figure **17**. Finish-machined samples showed the lowest surface roughness and smallest scatter; both white and green-machined samples showed considerably higher roughness with an increase of 57.6% and 51.1% in R_a and R_z, respectively for the white-machined samples and an increase of 40.8% and 40.1% in R_a and R_z, respectively for the green-machined samples. It should be noted that considering the scatter in data, the roughness obtained from the three different finishing procedures is not significant.

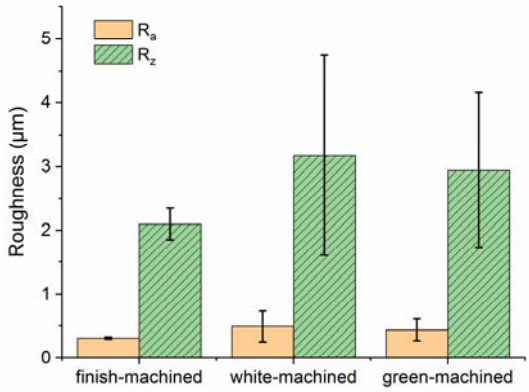

Figure 17. Surface roughness values for the three different surface-finish procedures.

The influence of the surface-finish procedure on the fatigue life was investigated by running cyclic 4PB tests at RT in air. The *S-N* curves obtained from the tests are shown in **Figure 18**.

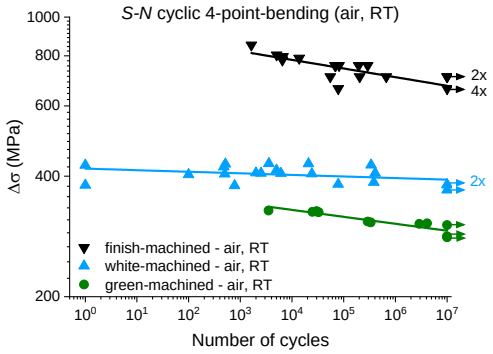

Figure 18. *S-N* curves from cyclic fatigue tests carried out in 4PB on bend bars with finish-machined, white-machined and green-machined surface finish.

The crack growth exponent *n* for these tests according to **Eq. (4**) is given in Table 5.

Table 5. Cyclic crack growth exponent according to **Eq. (4**) for samples with different surface-finish procedures.

Surface finish	***n*** **[-]**
Finish-machined, air, RT	46.3
White-machined, air, RT	253.8
Green-machined, air, RT	57.6

5. Discussion

In this work, a tailored grade of silicon nitride ceramic designed for the fabrication of ceramic springs was tested to characterize its mechanical properties and fatigue behavior. The CSR tests on finish-machined (i.e., ground) bars (refer to Table 2) revealed rather high Weibull moduli under various load rates at RT and 1000 °C, thus, suggesting small scatter in strength and pointing out to promising mechanical properties. The same data showed an expected reduction in strength with increasing temperatures, which may be attributed to the weakening of the secondary glassy phase at high temperatures; **Figure 7**. Although stiffness and strength are not directly scalable, the decline in stiffness beyond 800 °C (**Figure 6**) confirms the weakening of the glassy phase especially beyond the glass transition temperature. A reduction in strength with decreasing load rates was also observed, thus, pointing out to the presence of subcritical crack growth (SCG). An exception to this trend was observed in the tests carried out at 1000 °C at low load rates, whereby the samples tested between 4 N/s and 0.04 N/s showed insignificant change in the mean value of strength (Table 2). Hence, a load-rate threshold below which no measureable reduction in strength appears to exist. Since the load rate is a time-dependent variable, this

behavior suggests that the degradation process leading to SCG has reached saturation after a certain exposure time. The insignificant change in strength between 4 N/s and 0.04 N/s though may also be attributed to other factors such creep at extremely low load rates or merely due to the scatter of data. It is worth mentioning that published results [63] indicate more susceptibility of oxide ceramics (zirconia and alumina) to SCG at low temperatures than non-oxide ceramics (silicon nitride and silicon carbide).

Similar to the data obtained from the CSR tests on finish-machined bars, the cyclic fatigue results (*S-N* curves shown in **Figure 11**) reveal lower fatigue strength at 1000 °C compared to RT. The predominant intergranular fracture at HT and the presence of glassy phase residues on the detached grains (**Figure 14b**) can be attributed to the weakening of the glassy phase, which resulted in strength deterioration and eventual failure. On the other hand, the RT tests confirmed a reduction in fatigue strength under water compared to air. It has been established that water (also in the form of humidity in the atmosphere) interacts with strained silica and alumina bonds [64, 65, 47], in the form of a chemisorption process that occurs at crack tips, thus, resulting in stress corrosion cracking under constant [66] and cyclic load [33]. Although tested at a load ratio of R=0.1, fracture debris was present on the inspected fracture surfaces (**Figure 14**), which may have contributed to crack propagation during crack closure due to wedging as reported by Reece et al. [34].

In terms of component testing, the helical springs showed higher crack growth exponent and higher fatigue strength than both the 4PB samples and the disk springs, yet with considerable scatter in the data (**Table 4** and **Figure 12a** and **b**). Crack growth in ceramics depends on several factors such as surface crack size and form, material composition, loading mode and load ratio in addition to the environment. Hence, in components undergoing triaxial stresses, it is difficult to pinpoint the exact factors dominating the crack growth behavior.

The rather high fatigue strength observed in helical springs may be traced back to the small volume of material under stress; the opposite holds true for disk springs. This value is reflected by the effective volume, given by **Eq. (9)**, which incorporates both the geometry of the component and the stress distribution. It appears from the values obtained for the 4PB bars ($V_{eff,4PB}$=5.68 mm^3), the helical springs ($V_{eff,helical}$=0.23 mm^3) and the disk springs ($V_{eff,disk}$=23.60 mm^3) that the helical springs exhibit the smallest effective volume of these three geometries. This value obtained from the three-dimensional simulation model of the helical spring is somewhat expected given that the maximum tensile stresses are (i) confined to a minute volume in the vicinity of the machined side surfaces of the wire cross section

(**Figure 9**) and (ii) maintain a steep gradient towards the center of the wire cross section; both of which factors influence the value of the effective volume according to **Eq. (33)**.

The relatively large scatter in fatigue strength data obtained for helical springs is due to the intrinsic complexity of the machining and surface finishing and consequently, possible discrepancy in the surface quality of the individual samples. Although SEM ceramographic cross-sectional analysis and inspection of the ground surfaces of the springs did not reveal the presence of large surface defects or cracks (Figure **15**), it has been shown in a previous study [27] that natural flaws in ceramic components (e.g., processing and machining-induced flaws) are extremely difficult to identify by means of microscopy. The presence of machining induced flaws may, however, explain the relatively large number of springs failing during the first 100 loading cycles in fatigue tests. Another explanation for the scatter in fatigue data may be linked to the stress distribution in the component. A reduction in the Weibull modulus *m* (a parameter known to be material-dependent) and hence, an increase in the scatter of strength was separately reported by Fett et al. [67] and Hegedűsová et al. [68] for silicon nitride samples under steep stress gradients (due to contact loading) compared to identical samples under gradual stress gradients (in 4PB tests). As mentioned earlier, the loaded helical springs maintain steep stress gradients that may explain the large scatter in fatigue data. Here, it should be noted that helical springs mainly undergo shear stresses, whereas, in comparison, disk springs appear to have a much larger volume under tensile stresses (**Figure 10**).

The surface-finish procedure had a pronounced influence on the fatigue strength of the tested bend bars (**Figure 18**). The finish-machined samples showed superior strength in comparison to both white-machined and green-machined ones. The latter suffered the lowest strength as depicted in the *S-N* curve shown in **Figure 18**. The procedures followed in preparing the white and green-machined samples may have induced surface flaws that did not heal during the sintering process. It is also possible that the sintering process itself may give rise to cracks or cause surface flaws to propagate under the effect of thermal stresses. The suboptimal surface finish observed in the white and green-machined samples (**Figure 16b** and **c**) has weakened the samples. Besides surface morphological effects, the chemistry and the fracture toughness of the sintered surface often differs from those of the bulk material. The resulting sintering skin has affected the fatigue behavior of white and green-machined samples, whereas post-sintering ground samples do not suffer such a disparity between surface and bulk properties. Specific machining parameters such as the directionality, grit size, depth of cut, etc. strongly affect the strength of ceramics as detailed in the work of Quinn et al. [69].

While the quality of machining of side surfaces and edges in helical springs appears to be crucial, particular attention should be given to the surface integrity of the contact surface edges in disk springs due to the presence of the highest tensile stresses at these locations. This is particularly indispensable when disk springs are used in stacks to meet prescribed load and deflection requirements, which may even give rise to additional frictional stresses at contact surfaces.

Ceramic springs made of silicon nitride are promising for application at high temperatures as they withstand operating temperature limits far beyond those of steel springs. By relying on proper methods and tools, the design, processing and manufacturing of ceramic springs may be adapted to improve their reliability and prolong their service life.

6. Summary

In this study, material characterization of a tailored grade of silicon nitride based ceramic and component tests on ceramic springs were conducted. The following is a summary of the findings:

- The HT constant stress-rate (CSR) tests on bend bars indicated subcritical crack growth (SCG) between load rates of 4 N/s and 200 N/s resulting in decrease in strength with decreasing load rate. The CSR test data indicated insensitivity to load rates below 4 N/s down to 0.04 N/s, thus, implying saturation of the SCG effect at around 4 N/s or suggesting other factors related to the scatter of data or the presence of creep. The tests carried out at RT revealed slight increase in strength with increasing load rate throughout the load rate range under consideration.
- A comparison of the HT fatigue behavior between the bend bars, helical springs and disk springs revealed the highest crack growth exponent for the helical springs followed by the bend bars then the disk springs. Similarly, the fatigue strength was highest for the helical springs followed by the bend bars then the disk springs. This was traced to the fact that the effective volume, whose value depends on the volume of material under tensile stresses, was smallest for helical springs and largest for disk springs.
- The complexity level of the machining process was most challenging for helical springs. This was manifested by a relatively large scatter in fatigue data and a large number of samples failing during the first 100 loading cycles. Although mostly due to disparity in surface quality, this large scatter may also be attributed to the steep stress gradients developing in the loaded helical springs.
- Special care must be taken in machining the side surfaces and the edges of helical springs and the contact surface edges of disk springs. The surface integrity of the contact surfaces in disk springs, which bear the highest tensile stresses, is decisive in defining the service life of these components.

- The three finishing procedures studied on bend bars revealed that finish-machined samples, which were ground after sintering, had the smoothest surface finish and the most favorable fatigue behavior. Both white-machined (pre-fired, compressed, ground and then fully sintered) and green-machined (ground in the green-body state then fully sintered) samples showed comparable surface roughness values with a favorable fatigue behavior for the former.
- This study demonstrates the possibility of producing ceramic springs, which satisfy broad application regime requirements, with sufficient strength and fatigue resistance and the potential of improving their reliability by adopting proper design and testing tools and methods.

Acknowledgment

The research leading to these results has received funding from the Federal Ministry for Economic Affairs and Energy of the Federal Republic of Germany under grant agreement no. 19125 BG. The authors would also like to thank the Verband der Deutschen Federindustrie e.V. VDFI for their much appreciated technical support.

References

[1] A. Ziebell, O. Schöppl, R. Haubner and T. Konegger, "Identification of bearing defects in hybrid thrust ball bearings by vibration analysis," *Materials Science Forum,* Vols. 825-826, pp. 844-851, 2015.

[2] S. Strobl, F.-A. Adlmann, P. Supancic, T. Lube, R. Danzer and O. Schöppl, "Fracture toughness of silicon nitride balls via thermal shock," *Journal of the European Ceramic Society,* vol. 38, no. 4, pp. 1278-1287, 2018.

[3] I. Durazo-Cardenas, A. Starr, R. Sousa, J. Ferreira, A. Mota, M. Kram, G. Hughes, P. Bytnar and F. Bel, "Towards health monitoring of hybrid ceramic bearings in aircraft starter/generators," *Procedia Manufacturing,* vol. 19, pp. 50-57, 2018.

[4] R. Raga, I. Khader, Z. Chlup and A. Kailer, "Damage progression in silicon nitride undergoing non-conforming hybrid cyclic contact," *International Journal of Fatigue,* vol. 105, pp. 97-110, 2017.

[5] R. Raga, I. Khader, Z. Chlup and A. Kailer, "Experimental and numerical investigation of crack initiation and propagation in silicon nitride ceramic under rolling and cyclic contact," *Journal of Physics: Conf. Series,* vol. 843, p. 012030, 2017.

[6] K. Kida, J. Koga and E. C. Santos, "Crack growth and splitting failure of silicon nitride ceramic balls under cyclic pressure loads," *Mechanics of Materials,* vol. 106, pp. 58-66, 2017.

[7] W. Wang, H. Wen, N. He and W. Chen, "Effect of load on tribological properties of silicon nitride/steel under rolling-sliding contact condition," *Tribology International,* vol. 125, 2018.

[8] H. Shi, Z. Liu, X. Bai, Y. Li and Y. Wu, "A theoretical model with the effect of cracks in the local spalling of full ceramic ball bearings," *Applied Sciences,* vol. 9, no. 4142, 2019.

[9] B. Zhao, I. Khader, R. Raga, G. Konrath, U. Degenhardt and A. Kailer, "High temperature tribological properties of silicon nitride in dry sliding contact against Inconel 718 heated by laser," *Wear,* vol. 203000, pp. 434-435, 2019.

[10] B. Zhao, I. Khader, R. Raga, U. Degenhardt and A. Kailer, "Tribological behavior of three silicon nitride ceramics in dry sliding contact against Inconel 718 over a wide range of velocities," *Wear,* Vols. 448-449, p. 203206, 2020.

[11] Z. Badran, X. Struillou, F. Hughes, A. Soueidan, A. Hoornaert and M. Ide, "Silicon nitride (Si3N4) implants: The future of dental implantology?," *Journal of Oral Implantology,* vol. 43, no. 3, pp. 240-244, 2017.

[12] M. Rahaman and W. Xiao, "Silicon nitride bioceramics in healthcare," *International Journal of Applied Ceramic Technology,* vol. 15, no. 4, pp. 861-872, 2018.

[13] F. Mussano, T. Genova, L. Munaron, M. Giulia Faga and S. Carossa, "Ceramic Biomaterials for Dental Implants: Current Use and Future Perspectives," in *Dental Implantology and Biomaterial*, M. Almasri, Ed., Rijeka, IntechOpen, 2016.

[14] V. Franco Steier, C. Koplin and A. Kailer, "Influence of pressure-assisted polymerization on the microstructure and strength of polymer-infiltrated ceramics," *Journal of Materials Science,* vol. 48, pp. 3239-3247, 2013.

[15] P. Francisco Cesar, A. Della Bona, S. Scherrer, M. Tholey, R. van Noort, A. Vichi, R. Kelly and U. Lohbauer, "ADM guidance - Ceramics: Fracture toughness testing and method selection," *Dental Materials,* vol. 33, no. 6, pp. 575-584, 2017.

[16] A. Moradkhani, H. Baharvandi and A. Naserifar, "Fracture toughness of 3Y-TZP dental ceramics by using Vickers indentation fracture and SelNB methods," *Journal of the Korean Ceramic Society,* vol. 56, no. 1, pp. 37-48, 2019.

[17] G. Stachowiak and G. Stachowiak, "Wear behaviour of ceramic cutting-tools," *Key Engineering Materials,* vol. 96, pp. 137-164, 1994.

[18] B. Kramer, "On tool materials for high speed machining," *Journal of Engineering for Industry,* vol. 109, no. 2, pp. 87-91, 1987.

[19] S.-T. Buljan and S. Wayne, "Wear and design of ceramic cutting tool materials," *Wear,* vol. 133, no.

2, pp. 309-321, 1989.

[20] J. Vleugels and O. van der Biest, "Chemical wear mechanisms of innovative ceramic cutting tools in the machining of steel," *Wear,* vol. 225–229, p. 285–294, 1999.

[21] R. Silva, J. Gomes, A. Miranda and J. Vieira, "Resistance of Si3N4 ceramic tools to thermal and mechanical loading in cutting of iron alloys," *Wear,* vol. 148, no. 1, pp. 69-89, 1991.

[22] I. Khader, A. Renz and A. Kailer, "A wear model for silicon nitride in dry sliding contact against a nickel-base alloy," *Wear,* vol. 376–377, pp. 352-362, 2017.

[23] A. Renz, I. Khader and A. Kailer, "Tribochemical wear of cutting-tool ceramics in sliding contact against a nickel-base alloy," *Journal of the European Ceramic Society,* vol. 36, no. 3, pp. 705-717, 2016.

[24] B. Zhao, H. Liu, C. Huang, J. Wang, B. Wang and Y. Hou, "Cutting performance and crack self-healing mechanism of a novel ceramic cutting tool in dry and high-speed machining of Inconel 718," *The International Journal of Advanced Manufacturing Technology,* pp. 1-8, 2019.

[25] R. Danzer, "Ceramics: Mechanical performance and lifetime prediction," in *The Encyclopedia of Advanced Materials*, D. Bloor, R. J. Brook, M. C. Flemings, S. Mahajan and R. W. Cahn, Eds., Pergamon, 1994, p. 385–398.

[26] M. Lengauer and R. Danzer, "Silicon nitride tools for the hot rolling of high-alloyed steel and superalloy wires – Crack growth and lifetime prediction," *Journal of the European Ceramic Society,* vol. 28, no. 11, pp. 2289-2298, 2008.

[27] I. Khader and A. Kailer, "Damage mechanisms in silicon nitride wire-rolling tools: Lab-scale experiments and correlation with finite element modeling," *Journal of Materials Processing Technology,* vol. 210, no. 10, pp. 1314-1325, 2010.

[28] I. Khader, A. Hashibon, J.-M. Albina and A. Kailer, "Wear and corrosion of silicon nitride rolling tools in copper rolling," *Wear,* vol. 271, no. 9–10, pp. 2531-2541, 2011.

[29] A. Kailer, "Keramische Hochleistungswerkstoffe – Eigenschaften und Merkmale im Hinblick auf walztechnische Anwendungen," in *Walzen mit Keramik*, Stuttgart, Fraunhofer Verlag, 2009, pp. 23-32.

[30] I. Khader, A. Renz, A. Kailer and D. Haas, "Thermal and corrosion properties of silicon nitride for copper die casting components," *Journal of the European Ceramic Society,* vol. 33, p. 593–602, 2013.

[31] G. Roebben, J.-P. Erauw, T. Lube, R.-G. Duan, F. Cambier und O. Van der Biest, „Microstructure characteristics related to the high temperature fracture resistance of the ESIS silicon nitride reference material," A. Neimitz und I. Rokach, Hrsg., EMAS Publications, 2002, pp. 77-84.

[32] T. Kawakubo and K. Komeya, "Static and cyclic fatigue behavior of a sintered silicon nitride at room temperature," *Journal of the American Ceramic Society,* vol. 70, no. 6, pp. 400-405, 1987.

[33] D. S. Jacobs and I.-W. Chen, "Mechanical and environmental factors in the cyclic and static fatigue of silicon nitride," *Journal of the American Ceramic Society,* vol. 77, no. 5, pp. 1153-1161, 1994.

[34] M. Reece, F. Guiu and M. F. Sammur, "Cyclic fatigue crack propagation in alumina under direct tension-compression loading," *Journal of the American Ceramic Society,* vol. 72, no. 2, pp. 348-352, 1989.

[35] G. Choi, "Cyclic fatigue crack growth in silicon nitride: Influences of stress ratio and crack closure," *Acta Metallurgica et Materialia,* vol. 43, no. 4, pp. 1489-1494, 1995.

[36] C. J. Gilbert, R. H. Dauskardt and R. O. Ritchie, "Behavior of cyclic fatigue cracks in monolithic silicon nitride," *Journal of the American Ceramic Society,* vol. 78, no. 9, pp. 2291-2300, 1995.

[37] J. Chevalier, C. Olagnon and G. Fantozzi, "Subcritical crack propagation in 3Y-TZP ceramics: Static and cyclic fatigue," *Journal of the American Ceramic Society,* vol. 82, no. 11, pp. 3129-3138, 1999.

[38] T. Lube, I. Khader, A. Kailer, U. Degenhardt und K. Berroth, „Ermüdungsbruch in Siliziumnitrid," S. Mayer, M. Panzenböck und H. Clemens, Hrsg., Bonn, Praktische Metallographie Sonderband, INVENTUM GmbH, 2014, pp. 353-357.

[39] I. Khader, S. Rasche, T. Lube, R. Raga, U. Degenhardt and A. Kailer, "Lifetime prediction of ceramic components – A case study on hybrid rolling contact," *Engineering Fracture Mechanics,* vol. 169, pp. 292-308, 2017.

[40] N. Koiso, A. Tsuchiya and H. Usui, "Influence of sintering skin layer of silicon nitride on proof testing effect," *Transactions of the Japan Society of Mechanical Engineers Series A,* vol. 62, no. 604, pp. 2657-2662, 1996.

[41] R. Danzer, "On the relationship between ceramic strength and the requirements for mechanical design," *Journal of the European Ceramic Society,* vol. 34, no. 15, pp. 3435-3460, 2014.

[42] R. Ritchie, "Mechanisms of fatigue crack propagation in metals, ceramics and composites: Role of crack tip shielding," *Materials Science and Engineering, A,* vol. 103, pp. 15-28, 1988.

[43] R. Ritchie und M. Launey, „Crack growth in brittle and ductile solids," in *Encyclopedia of Tribology*, Q. J. Wang und Y. Chung, Hrsg., Boston, MA, Springer US, 2013, pp. 596-605.

[44] R. H. Dauskardt, "A frictional-wear mechanism for fatigue-crack growth in grain bridging ceramics," *Acta Metallurgica et Materialia,* vol. 41, no. 9, p. 2765–2781, 1993.

[45] S.-Y. Liu, I.-W. Chen and T.-Y. Tien, "Fatigue crack growth of silicon nitride at 1400°C: A novel fatigue-

induced crack-tip bridging phenomenon," *Journal of the American Ceramic Society,* vol. 77, no. 1, pp. 137-142, 1994.

[46] G. Grathwohl and T. Liu, "Crack resistance and fatigue of transforming ceramics: I, materials in the ZrO2–Y2O3–Al2O3 system," *Journal of the American Ceramic Society,* vol. 74, no. 2, pp. 318-325, 1991.

[47] T. A. Michalske and S. W. Freiman, "A molecular mechanism for stress corrosion in vitreous silica," *Journal of the American Ceramic Society,* vol. 66, no. 4, pp. 284-288, 1983.

[48] "DIN EN 843-1: Advanced technical ceramics - Mechanical properties of monolithic ceramics at room temperature - Part 1: Determination of flexural strength," Beuth Verlag GmbH, Berlin, 2008.

[49] "DIN EN 843-4: Advanced technical ceramics - Mechanical properties of monolithic ceramics at room temperature - Part 4: Vickers, Knoop and Rockwell superficial hardness," Beuth Verlag GmbH, Berlin, 2005.

[50] "DIN EN 843-2: Advanced technical ceramics - Mechanical properties of monolithic ceramics at room temperature - Part 2: Determination of Young's modulus, shear modulus and Poisson's ratio," Beuth Verlag GmbH, Berlin, 2007.

[51] D. Munz and T. Fett, Ceramics: Mechanical Properties, Failure Behaviour, Materials Selection, vol. 36, Springer, 1999.

[52] T. Fett and D. Munz, "Chapter 9.5 - Fracture Mechanics," in *Handbook of Advanced Ceramics*, 2nd ed., S. Shigeyuki, Ed., Amsterdam, Academic Press, 2013, pp. 681-715.

[53] R. Jain, Effective area and effective volume calculations for ceramic test specimens, PhD Thesis, Cleveland, Ohio: Cleveland State University, 2008.

[54] "DIN 2090: Helical Compression Springs made of Flat Bar Steel; Calculation (Zylindrische Schraubendruckfedern aus Flachstahl; Berechnung)," Beuth Verlag GmbH, Berlin, 1971.

[55] W. Beckert, J. Stockmann and C. Koplin, "Auslegungsplattform für keramische Schraubendruckfedern," in *4. Ilmenauer Federntag*, Ilmenau, 2017.

[56] V. Kobelev, "Exact shell solutions for conical springs," *Mechanics Based Design of Structures and Machines,* vol. 44, no. 4, pp. 317-339, 2016.

[57] V. Kobelev, Durability of Springs, Cham: Springer, 2018.

[58] J. Marsden und T. Hughes, Mathematical Foundations of Elasticity, New York: Dover Publications, Inc., 1983.

[59] E. Ventsel and T. Krauthammer, Thin Plates and Shells. Theory, Analysis, and Applications, New York: Marcel Dekker, Inc., 2001.

[60] "DIN EN 16984: Disc springs - Calculation (Tellerfedern - Berechnung)," Beuth Verlag GmbH, Berlin, 2017.

[61] T. Fett, G. Martin, D. Munz and G. Thun, "Determination of da/dN-ΔK1 curves for small cracks in alumina in alternating bending tests," *Journal of Materials Science,* vol. 26, pp. 3320-3328, 1991.

[62] M. Härtelt, H. Riesch-Oppermann, T. Schwind and O. Kraft, "Statistical evaluation of fatigue crack propagation from natural flaws in silicon nitride," *Journal of the American Ceramic Society,* vol. 94, no. 10, pp. 3480-3487, 2011.

[63] A. Wojteczko, R. Lach, K. Wojteczko, P. Rutkowski, D. Zientara and Z. Pędzich, "Subcritical crack growth in oxide and non-oxide ceramics using the constant stress rate test," *Processing and Application of Ceramics,* vol. 9, no. 4, pp. 187-191, 2015.

[64] T. A. Michalske and B. Bunker, "Slow fracture model based on strained silicate structures," *Journal of Applied Physics,* vol. 56, no. 10, pp. 2686-2693, 1984.

[65] S. Wiederhorn, S. Freiman, E. Fuller and C. Simmons, "Effects of water and other dielectrics on crack growth," *Journal of Materials Science,* vol. 17, no. 12, pp. 3460-3478, 1982.

[66] W. Hongjie, W. Yonglan, J. Zhihao and Z. Huijiu, "The effect of the microstructure on the static fatigue behaviour of Si3N4," *Journal of Materials Science,* vol. 32, no. 21, pp. 5775-5778, 1997.

[67] T. Fett, E. Ernst, D. Munz, D. Badenheim and R. Oberacker, "Weibull analysis of ceramics under high stress gradients," *Journal of the European Ceramic Society,* vol. 23, no. 12, pp. 2031-2037, 2003.

[68] L. Hegedűsová, L. Ceniga and J. Dusza, "Bending and contact strength of monolithic ceramic materials," *International Journal of Damage Mechanics,* vol. 21, no. 2, pp. 293-305, 2012.

[69] G. Quinn, L. Ives and S. Jahanmir, "Machining cracks in finished ceramics," *Key Engineering Materials,* vol. 290, pp. 1-13, 2005.